Photogrammetric Modelling of Submerged Structures: Influence of Underwater Environment and Lens Ports on Three-Dimensional (3D) Measurements

Fabio Menna, Erica Nocerino and Fabio Remondino

3D Optical Metrology (3DOM) unit, Bruno Kessler Foundation (FBK), Trento, Italy; (fmenna, nocerino, remondino) @fbk.eu; http://3dom.fbk.eu

Abstract: Underwater three-dimensional (3D) measurements and modelling is gaining interest thanks to technological developments of diving equipment and underwater technologies. Also, in this environment, photogrammetry is regarded as competitive and flexible method, which may lead to impressive and valuable results at different depths and in a broad range of application fields. To guarantee fit-to-purpose digitization results, a deep understanding of the physical peculiarities of the underwater environment is crucial, equipment and tools, which rule the image formation and affect the quality of the results. This paper aims to address these topics, providing a brief overview of the main properties of water and deepening the optical behaviour of photographic apparatus underwater. The difference between dome and flat ports is investigated, both in terms of image quality, geometric calibration, and accuracy potential. The two ports are employed for the 3D modelling of a semi-submerged structure; the experimental results show lower metric performances of the flat port, with significant differences per colour channel.

Keywords: underwater photogrammetry; calibration; image aberrations; dome port; flat port

---

1. Introduction

Since remote times, mankind has been bound to water bodies, either in their natural forms, such as oceans, lakes, rivers, wetlands, or in their man-made counterparts, such as structures, flumes, channels, basins, dams, etc. Evidence of human life from the very beginning hides under the water level, off the coasts, under shallow seas or deep oceans, but also inland water bodies of countries all around the world. Consequently, underwater cultural heritage (UCH) is very vast, probably much more than one can imagine, encompassing wrecks, ruins, submerged landscapes, caves, and all traces of exploitation of marine resources. At

the same time, exploring, documenting, and measuring the underwater environment and submerged objects is gaining importance in many application fields, ranging from biological studies to monitor climate changes and man-induced environmental alterations, to the investigation, assessment, and exploitation of seabed mineral and oil deposits.

Accordingly, there is a clear need to develop efficient techniques and methods to face the challenges and problems of underwater prospection, documentation, and monitoring.

With these aims, underwater photogrammetry has gained a remarkable success over the last few years even using consumer grade photographic equipment (Balletti et al., 2015; Demesticha et al., 2014; Diamanti and Vlachaki, 2015; Menna et al., 2013). Indeed, diver operated underwater housings are available for a wide range of digital cameras, sometimes designed and sold by the manufacturer of the cameras themselves, sometimes from third-party companies. For applications where cameras are used at very great depth, specialised housings are manufactured ad hoc to resist the high pressures and are not operated by a diver but installed to AUV, ROV, or a submarine (Drap et al, 2015; Kwasnitschka et al, 2016; Roman and Mather 2010).

This contribution reports the current state of a research that the authors have been carrying out for several years and part of a wider project called OptiMMA (optical metrology for maritime applications, http://3dom.fbk.eu/projects/underwater-photogrammetry-maritime-applications) with the twofold aim of (i) investigating the accuracy potential of different optical sensors when immersed in water, and (ii) providing operational guidelines to meet predefined quality requirements.

Testing underwater photographic equipment and assessing the accuracy potential of cameras enclosed in a waterproof housing is even more crucial than in photogrammetry applications above the water, with additional difficulties given by the underwater environment. Although underwater accuracy requirements are generally less demanding, assessing and evaluating the quality of photogrammetric measurements underwater is yet necessary, albeit far from being an easy task, to guarantee a fit-to-purpose underwater three-dimensional (3D) acquisition.

Stating the peculiarities of the hostile underwater environment, probably even more than in air, a basic understanding of its physical characteristics, together with a deep knowledge of optical behaviour of underwater photographic equipment is fundamental for a successful approach to underwater photogrammetry.

The planning of an underwater photographic acquisition for photogrammetric purposes needs to be carried out considering water physical properties and conditions, directly (i.e., water turbidity, lighting conditions) or indirectly (i.e., currents, depth, temperature) influencing the quality of acquired images.

The knowledge about photographic equipment and its performances in different conditions is a further fundamental topic to be investigated. Photographic cameras normally used on land, above the water, need a special housing with a flat or dome port to be used also in water. Looking to the underwater scene through a flat or dome port has many optical consequences, of which the most known is that the field of view of the lens mounted on the camera is preserved in case of a dome port and reduced by a factor almost equal to the refractive index of water for the flat port. In general, this common rule is satisfied, but there are many other factors that intervene in the optical formation of the image, some with very important practical implications that may make the choice of a type of port with respect to another one not as trivial, as described above.

For instance, lenses that are used in photography are designed to minimise optical aberrations throughout the entire image format. Residual aberrations are always present and their amount is depending on the optical design, quality of glasses, and therefore cost of the lens.

Nowadays, even the cheap zoom kit, bundled with consumer cameras, provide an acceptable image quality for less demanding photogrammetric purposes. Nevertheless, when used underwater, behind flat and dome ports, image quality, even for the most expensive cameras, undergoes quite a visible degradation due to the modification of the entire optical design. Depending on the combination of lens and port used (spherical dome or flat), the consequences on the overall image quality may be disappointing.

Moving from these considerations, in the first part of this contribution, the main physical properties of water are explained in relation to how they affect underwater photography (section 2). Then, a brief, but necessary comparative analysis about how dome and flat ports influence an underwater photogrammetry project is provided (Section 3). The analysis is the result of literature review as well as computer simulations and tests carried out by the authors above the water in laboratory as well as underwater (in swimming pool and at sea). Underwater camera calibrations, as well as image quality analyses, are carried out with flat and dome ports using a specific test object designed by the authors (Section 4). The paper continues with experimental tests that aim to analyse the accuracy potential of underwater photogrammetry when working with minimum number of reference control measurements (i.e., ground control points and reference lengths): the tests are reported for an industrial archaeology 3D modelling project of a maritime heritage building (Section 5). A comparative analysis is carried out using a same camera and lens encased in a waterproof housing using both dome and flat ports. Then, the archaeological structure is surveyed twice using the same camera-lens-housing but mounting the dome port first and flat port after. Internal quality figures from the bundle adjustment and from comparison against measured reference lengths are reported and discussed.

2. The Underwater Environment

Seawater is about 800 times denser than air, and is characterised by an optical index of refraction that varies as function of temperature, salinity, pressure, and light wavelength (Austin and Halikas, 1976). All these quantities are correlated: density increases as temperature decreases, salinity increases as pressure increases, pressure increases linearly with depth (every 10 m the pressure increases of 1 atmosphere, equal to 1.033 N/cm^2).

The optical properties of seawater (Mobley, 1995) are highly variable and rule the propagation of light, consequently affecting all of the disciplines that entail optical measurements. Optical properties are usually divided into two classes: (i) the inherent properties, such as the absorption coefficient and volume scattering, which depend on the medium; and, (ii) the apparent optical properties (irradiance reflectance, attenuation coefficients, etc.) that are also functions of the light field, i.e., the way in which light particles (photons) travel in all directions through space.

According to the National Snow and Ice Data Centre (NSIDC), almost 94% of sunlight radiation that hits the sea surface penetrates and is then absorbed by water. The height of sun, depending on the location on Earth, time of day, and season, and the sea conditions influence the actual amount of light that is absorbed or reflected upward.

Figure 1. An underwater image of a rock in shallow water taken at noon (**left**) and later in the afternoon (**right**). Light caustics are visible in the left image.

Light is more absorbed in rough seas, whereas is highly reflected in calm waters that act as a mirror surface. Light rays are refracted by wavy surface, producing bright patterns, known as caustics, which are unfavourable for photogrammetric applications because they could affect the automatic extraction of two-dimensional (2D) features in images, as well as produce poor quality object texture. Figure 1 shows the same scene with (Figure 1-left) and without (Figure 1-

right) caustics. The intensity of light caustics depends on sun elevation, water turbidity and depth, with the effect that is significantly reduced already after few meter depth (Floor, 2005).

A major effect of water on light propagation is that it acts as a selective filter: the great amount of light entering the sea is absorbed or attenuated, i.e., it is converted in heat, within the first meters; only 1% of light entering the sea reaches 100 m. Not all of the components of light are absorbed at the same rate: both long (orange, red, and infrared) and short (ultra-violet) wavelengths are rapidly attenuated; green, and, especially, blue components penetrate more. Water composition affects the maximum depth at which light penetrates: in turbid coastal waters light hardly goes deeper than 20 m; while in open ocean blue light may even arrive at 200 m, depth limit after which there is almost no light.

The use of artificial light sources, such as strobes, is essential in underwater environment, especially in deep water, to restore the full range of colours, and compensate for light attenuation limiting the visibility range.

The presence in water of suspended particles (phytoplankton, organic matter, pollution, etc.) causes turbidity in water, and, that in turn, produces light scattering. Turbidity of water is generally quantified using the Secchi distance (Wernand, 2010; Cialdi and Secchi, 1865), an empirical method introduced in 1865 that makes use of a white circular disk. One Secchi distance is defined as the maximum depth or distance at which the disk is still visible.

Scattering or diffuse reflection is an optical phenomenon that arises when the light rays are randomly deviated from their straight paths. Scattering limits image quality, reducing the contrast and producing blurred images.

When strobes are used, also backscattering may occur; similar to scattering, the difference is that the light from the artificial source is reflected from the particles mainly back to the camera. To reduce backscattering, strobes should be carefully positioned, trying to keep the light cones of the strobes outside of the field of view of the camera as much as possible.

This translates in lightening the subject with the strobes far from the camera lens. The closer the flash to the camera, the more backscatter is produced. The closer to the subject the picture, the less water and particles between the camera and subject, and consequently, the less backscatter is produced.

From what has been highlighted above, the environment peculiarities heavily affect both the quality and how the images are to be acquired underwater. Turbidity is a remarkable limiting constraint, and scatter and backscatter reduce the contrast of the scene and the final quality of the image. Even in very clear water, the image acquisition can be difficult. Indeed, when a Secchi distance corresponds to several meters, a strong illumination would be required to light the object, and a wide baseline would be necessary between two lateral light sources and the camera lens to avoid backscatter. In extreme cases, a single diver might not be able to operate alone the system of cameras and strobe lights. An example of

this phenomenon is visible in Figure 2. Two underwater photographs are taken, respectively, with (Figure 2-left) and without the strobe (Figure 2-right). The prominent back scatter effect is here caused by the short strobe-to-lens distance (less than 1m) between the strobe and the camera lens while the object is 7-10 m away from the camera lens.

Figure 2. Back scatter effect (**left**) caused by a short strobe-to-lens distance. The same image taken in natural light, without strobes, results in a higher contrast and sharpness image (**right**).

3. Lens Ports for Underwater Photography

As well known among underwater photographers and photogrammetrists, lens ports, coupled with waterproof camera housings, are designed to be either flat or (hemi)spherical. Their different shape rules and highly changes the geometry of image formation underwater, consequently affecting the survey planning and image acquisition. Table 1 reports the main characteristics and differences between the two ports. The most remarkable differences are due to the planar shape of flat ports that acts as a separation surface between two media, i.e., water outside and air inside the waterproof housing, causing a deviation (refraction) of optical rays from the ideal path, according to Snell's law. Instead, the hemispherical ports are made of two spherical surfaces, having ideally the same centre of curvature that coincides with the centre of the lens (the so-called entrance pupil, EP, or perspective centre). The closest the EP to the centre of curvature of the port, the less the light rays are refracted, and thus the closer is the image to the hypothesis of central perspective geometry.

Table 1. Characteristics of flat and dome ports.

	Hemispherical Dome Port		**Flat Port**	
Description	Concentric lens acting as additional optical element (negative or diverging lens)		Flat plane of optically transparent glass or plastic	
Field of view (FOV) WRT the camera-lens system	Equal	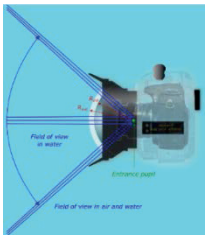	Reduced	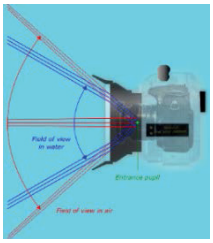
Focal length WRT the camera-lens system	Equal		Increased (by a factor equal to approximately the ratio between the refraction indices of water and air)	
Magnification WRT the camera-lens system	Equal		Increased (by a factor equal to approximately the ratio between the refraction indices of water and air)	
Effect on the observed object	An upright, smaller virtual image of the object is formed at a distance from the dome surface equal to 3 times the curvature radius of the dome. The camera-lens system focuses on this virtual image.		The object appears closer to the camera by a factor of about 25%, i.e., approximately the reciprocal of the refraction index of water.	
Maximum FOV	Not limited		Limited to 96°	
Lens distortion	No significant distortion		Pincushion distortion	
Other effects	• Increase of Depth of field (DOF) by a factor equal to approximately the ratio between the refraction indices of water and air • Spherical aberration • Field curvature		• Chromatic aberration. • Astigmatism	
Costs	More expensive		Cheaper	
Typical use	For DSLR cameras		For compact digital cameras	

4. Underwater Equipment Calibration

The first step in the experimental work consists of the calibration of the photographic system made of a digital camera, plus lens in a waterproof housing with both dome and flat ports (Section 4.1) to assess its optical quality and accuracy potential. The tests are performed on a portable test object (Section 4.2), which is specifically designed by the authors, made of three Dibond® aluminium composite sheets with a thickness of 3 mm. The image quality of two systems, one

equipped with the dome port and the other with the flat port, is analysed (Section 4.3.1). Finally, their accuracy potential is assessed comparing the results of self-calibration with respect to measurements that are derived from the calibration of the camera-lens system in air (Section 4.3.2).

4.1. Photographic System

A Nikon D750 24 Mpx full frame camera (pixel size 5.97 μm) mounting a Nikkor AF 24mm f2.8/D wide angle lens was put in a NiMAR NI3D750ZM pressure housing. The system is shown in Figure 3. In order to guarantee the highest accuracy, each image acquisition was carried out with a fixed focus set for the first image of the sequence. The distance to the object was kept constant through both of the visual references and using ropes with marks. Between the two underwater surveys just the port was changed and then the adjustment of the focus done. A Nikon SB700 strobe mounted in a dedicated NiMAR housing was used for the underwater calibrations.

Figure 3. Nikon D750 camera, Nikkor AF 24 mm f/2.8D, NiMAR NI3D750ZM pressure housing and the two different ports used (from left to right).

4.2. Underwater Test Object

The test object (Figure 4) is made of three Dibond® aluminium composite sheets with a thickness of 3 mm. The Dibond® material consists of 2 layers of 0.3mm thick aluminium sandwiching a core containing UV stabilized virgin low density polyethylene (http://alucobond.com.au/specify-now/dibond/#sthash.uKarrJ0o.dpuf). The three panels, sided together, form a 1500x1000mm^2 board, fixed on the back to a structural frame made with Rexroth aluminium profiles, which add rigidity and mechanical stability to the structure. To provide the structure with depth variation that is suitable for photogrammetric camera calibration, six square plates with additional targets can be mounted using optical breadboard support rods made of stainless steel, currently up to 200 mm long. The linear thermal expansion coefficient of Dibond® panels is 0.024 mm/(m·K). A total of 160 circular coded targets, designed with a black square background that allows for MTF measurements, are regularly distributed over the test object. Other resolution wedges and colour checkboards are also present.

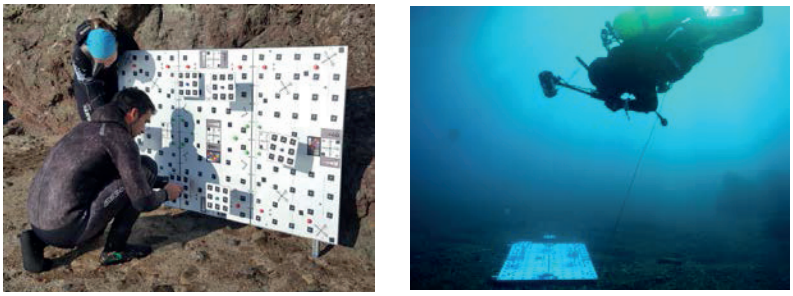

Figure 4. The test object used for underwater calibrations during the assembly (**left**) and image acquisition (**right**).

4.3. Underwater Camera Calibrations

The portable test object is laid down at a depth of about five meters and photographed from an average distance of about 1.2 m for the dome port and 1.6m for the flat port, providing a ground sampling distance (GSD) of about 0.3mm for both of the calibrations. An aperture value of f/11 is used for both the flat and dome ports. About 30 images per each port are collected, using a standard self-calibration protocol with multi-view convergent images and roll diversity (Fraser, 1997). The image acquisitions are carried out in sequence, the dome port first and the flat port after.

4.3.1. Analysis of Image Quality

As expected, from a visual analysis of the acquired images, it is easily recognisable that, while the dome port preserves the barrel distortion of the lens almost unchanged, (Figure 5-centre), the flat port introduces a heavy pincushion distortion (Figure 5-bottom). Furthermore, the image quality for the flat port is severely different between the centre (Figure 6a) and the corners, showing some heavy chromatic aberrations (Figure 6b) and blur astigmatism, different per red, green, and blue channels, with the blue channel behaving the worst (Figure 6c–e).

Above Water No Port

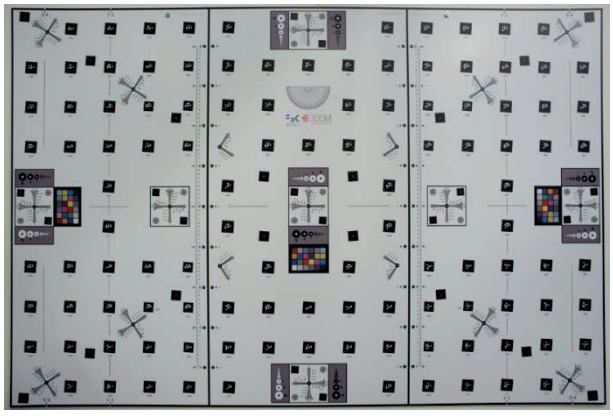

UW Dome Port

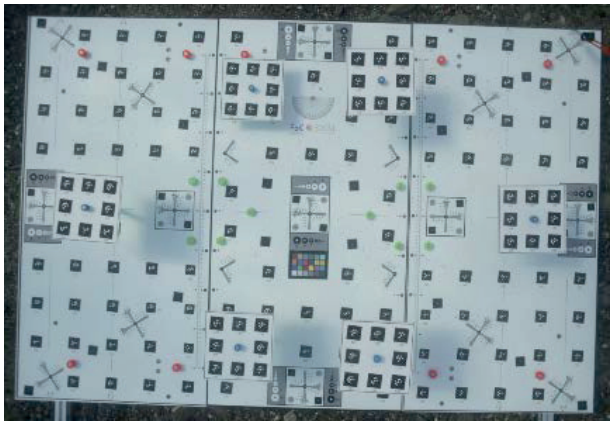

UW Flat Port

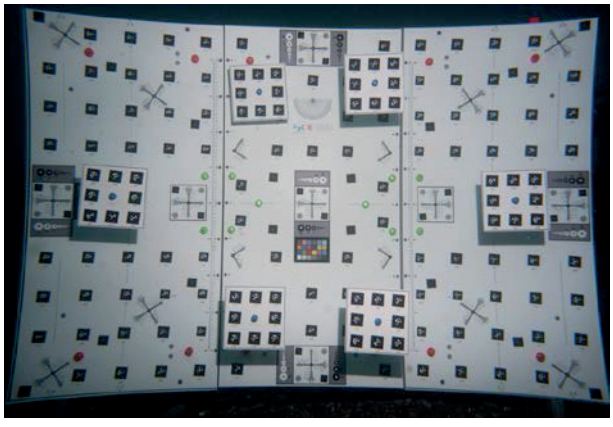

Figure 5. The portable test object as imaged above the water without the pressure housing (up), underwater with the dome port (centre) and flat port (bottom).

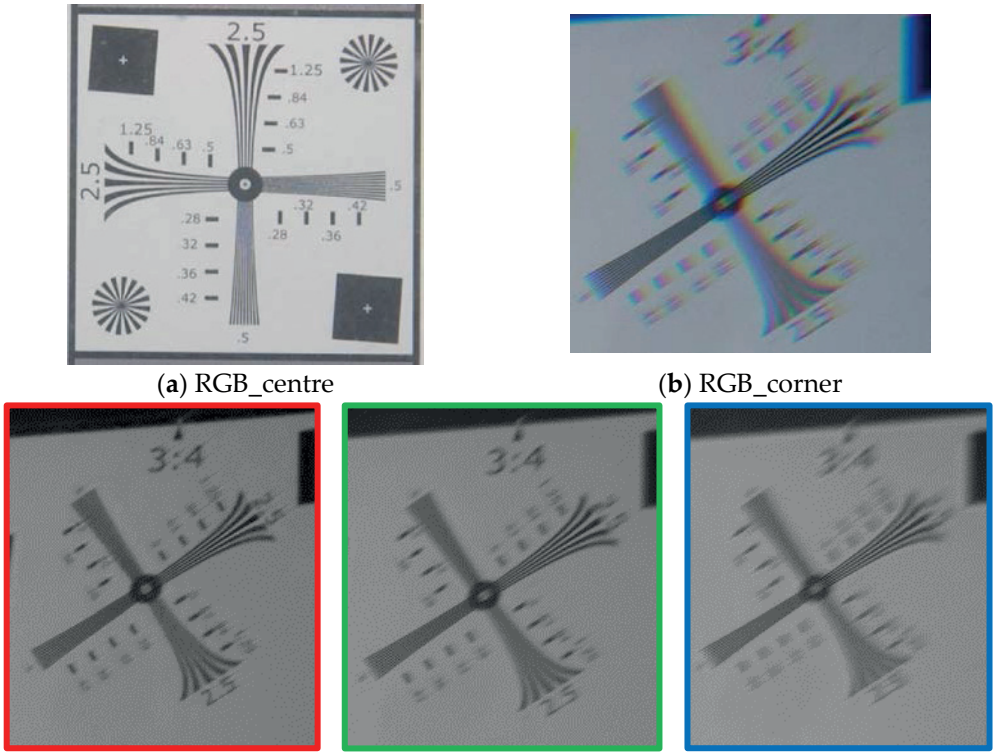

(**a**) RGB_centre (**b**) RGB_corner

(**c**) RED_corner (**d**) GREEN_corner (**e**) BLUE_corner

Figure 6. Visual image analysis for the flat port. Resolution patches respectively at the centre (**a**) and at the corner (**b**) of the field of view as seen in the colour image. Single red (**c**), green (**d**), blue (**e**) channels at the corner of the image displaying a colour dependant astigmatism.

Figure 7 shows three resolution patches that are placed along a diagonal (first quadrant) of the test object, respectively, in the centre, at 2/3 of maximum radius and at corner both for the dome and flat ports. All of the underwater images display a reduction in contrast; however, while the centre patch is well resolved, going towards the upper right corner results in a significant worsening of image quality for both dome and flat ports. Especially at the corner, the dome port shows some blur due to field curvature, while the flat port shows severe chromatic aberrations and blur due to astigmatism already at half of the maximum radial distance. Note how for the flat port the astigmatism is colour dependent. To visually highlight this behaviour for the flat port, Figure 6 also shows for the upper right corner patch, the red, green, and blue channels. For the red channel, a slight astigmatism makes tangential limiting resolution (stripes with tangential edges) worse than the radial one. A cross section extracted at subject resolution of 1.25 mm still shows a good reproduction of the signal that is instead flattened for the blue channel.

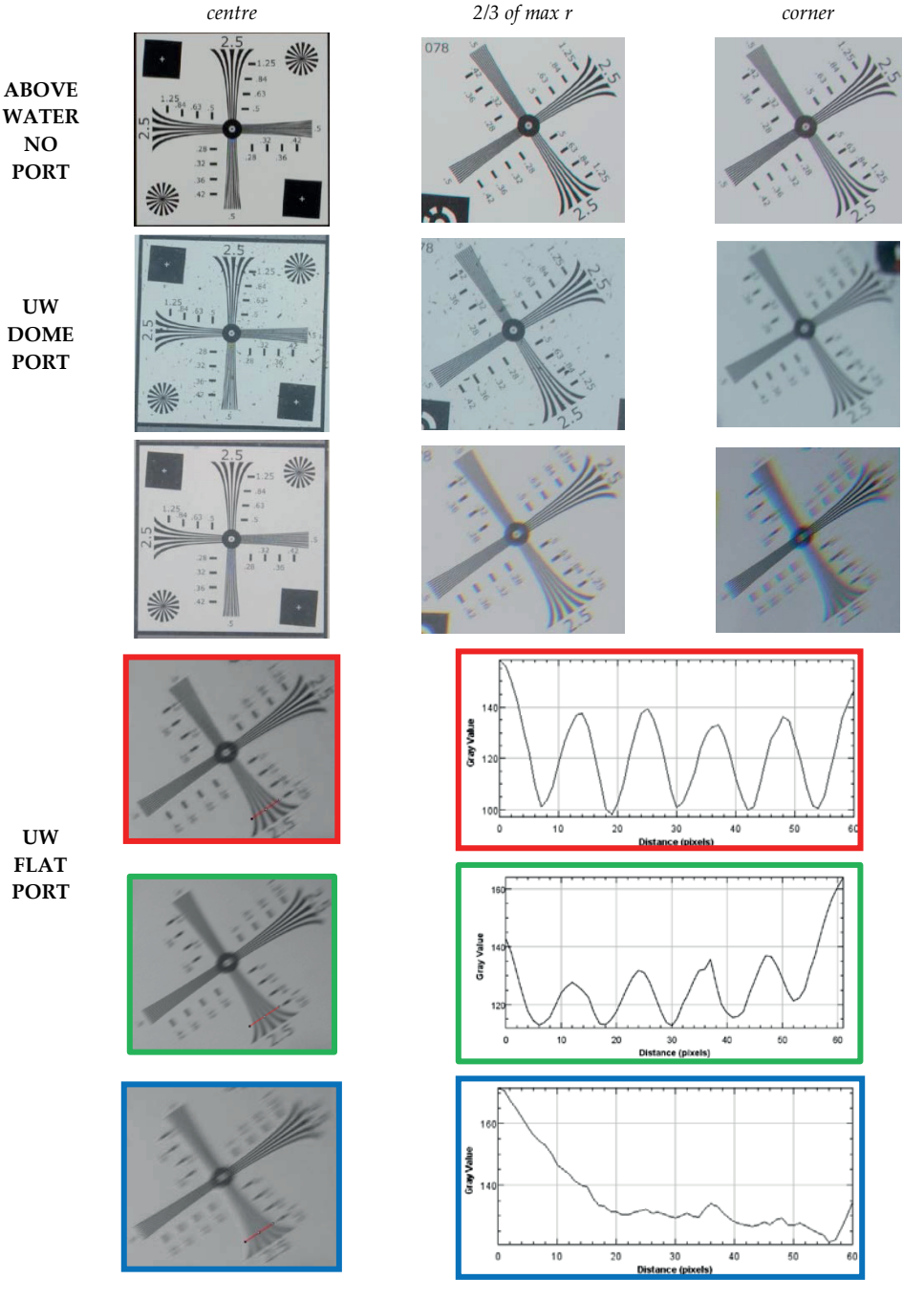

Figure 7. Resolution patches as imaged above the water without the pressure housing, with the dome port and with the flat port. For the flat port, a section along the radius is reported for the red and blue channels showing a colour-dependent astigmatism.

4.3.2. Geometric Calibration

The two underwater datasets and the reference in air (or above water) dataset are processed using the open source damped bundle adjustment toolbox (DBAT) v0.6.2.0 (Börlin and Gussenmeyer, 2013) for MATLAB environment. The least squares method implemented in PhotoModeler for the automatic marking of circular coded targets is employed. The method extracts the target centroids in the green channel as default. Table 2 synthetically summarises the results of the calibration processing. As it can be noted, the flat port performs quite significantly worse than the dome port, which displays a higher potential accuracy (image observation from green channel for both ports).

Table 2. Results of self-calibrating bundle adjustment: interior orientation and additional parameters are reported along with internal assessment in image and object space.

	D750-24mm *No Port* above Water Calibration	**D750-24mm *Dome Port* UW Calibration**	**D750-24mm *Flat Port* UW Calibration**
Principal distance c [mm]	24.624 ± 4.7e-004	26.001 ± 0.001	33.110 ± 0.004
Principal point ppx [mm]	0.0391 ± 5.5e-004	-0.0437 ± 0.002	-0.0831 ± 0.005
Principal point ppy [mm]	0.0158 ± 5.0e-004	-0.1486 ± 0.002	-0.1341 ± 0.005
k1 [mm^{-2}]	1.649e-004 ± 2.2e-007	1.679e-004 ± 7.3e-007	-1.965e-004 ± 9.5e-007
k2 [mm^{-4}]	-2.461e-007 ± 1.2e-009	-2.873e-007 ± 5.7e-009	-1.917e-007 ± 5.8e-009
k3 [mm^{-6}]	2.593e-011 ± 2.0e-012	2.200e-010 ± 1.3e-011	1.943e-010 ± 1.0e-011
P1 [mm^{-1}]	-3.506e-006 ± 3.4e-007	-8.022e-006 ± 7.9e-007	4.445e-005 ± 2.9e-006
P2 [mm^{-1}]	-1.233e-006 ± 2.9e-007	3.168e-005 ± 7.4e-007	8.984e-005 ± 2.6e-006
Re-projection error RMS [pixel]	0.21	0.32	0.91
Point error vector length RMS [mm]	0.03	0.06	0.12
Point error vector length maximum [mm]	0.10	0.22	0.30
Relative precision (wrt a maximum dimension of 1800 mm)	≈1:62000	≈1:29000	≈1:15000

From the output of bundle adjustments with self-calibration (Brown model formulation with radial and decentring distortions), we can highlight the following considerations:

- the obtained precisions of interior orientation parameters for dome and flat ports are considerably poorer than laboratory calibration. The flat port performed significantly worse than the dome port with a standard deviation of the principal distance 4 times greater than the dome port and nine times

greater than the laboratory calibration;

- a higher potential accuracy for the dome port with respect to the flat port (image observation from green channel for both ports) is notable;
- the principal point for both dome and flat ports is significantly different with respect to the one computed above water without the pressure housing. In particular, the principal point variation in y is systematically greater towards the negative values, probably caused by a camera misalignment in the pressure housing;
- the RMS of image residuals for the flat port is three times greater than the dome port and more than four times with respect to the above water calibration; and,
- as expected, due to the effect of refraction, the principal distance of the imaging system with the flat port is about 34% greater than the above the water calibration.

The accuracy assessment is carried out using 23 known distances on the three panels of the test object. The influence of deformations of the panels are taken into account so that only those lengths whose potential errors (chord against arc distance) are below 15 μm are considered.

According to Luhmann et al (2014), the theoretical length measurement error (TLME) and the length measurement error (LME) are defined as follows:

$$\mathrm{TLME} = 3\sqrt{2} \cdot s_{XYZ} \tag{1}$$

$$\mathrm{LME} = D_m - D_r \tag{2}$$

where S_{xyz} are the standard deviations of object coordinates, and $D_{r,m}$ are the reference and measured distances, respectively. Table 3 summarises the length measurement error (LME) for the dome port and flat port; it is computed according to (2) as the difference between the measured distance D_m for the dome and flat ports, and the distance from the above water calibration, assumed as reference length D_r. For the underwater tests reported in this paper, the theoretical length measurement error (TLME) of the reference at 99% confidence level is 0.078mm. The relative length measurement accuracy (RLMA) is defined as:

$$\mathrm{RLMA} = 1 : ROUND\left(\left|D_r / (D_m - D_r)\right|\right) \tag{3}$$

Table 3. Length measurement error for the underwater bundle adjustment results.

	D750-24mm *Dome Port* UW Calibration	**D750-24mm *Flat Port* UW Calibration**
LME [mm]	0.082	0.212
RLMA (wrt to the maximum reference length of 900 mm)	≈1:11000	≈1:4250

5. Real Case Scenario Experiment

The two underwater photographic systems are tested in a real case scenario to quantify the effect of image quality and camera calibration that is analysed in Section 4 when dealing with the 3D modelling project of underwater heritage.

5.1. The Modelled Heritage Structure

A semi submerged industrial structure of about 20x10m^2 located in the Bay of Rogiolo, near Livorno, Italy, today abandoned and under consideration for restoration (Figure 8), is used as test site. Originally, the structure was a harbour, serving as support for cave and cement plan activities at the beginning of the twentieth century. A combination of close range photogrammetry above and under the water according to the procedure described in Menna et al. (2015, 2013) is chosen for modelling the structure. The part of the structure underwater is photographed twice, once with the dome port and a second time with the flat port. During the survey, the sky was overcast limiting the water caustics effect on the underwater structures.

Figure 8. The surveyed port structure in the bay of Rogiolo near Livorno, Italy. At the top row, historical images of the bay and the industrial structure (Ciompi, 1991).

5.2. Targeting of the Industrial Structure

Eight plates with eight coded target are each placed across the waterline (Figure 9-a) of the rectangular basin chosen to perform the comparative photogrammetric tests (Figure 9-b).

The coded targets are placed for the twofold aim of: (i) allowing to register the underwater and above the water 3D models, and (ii) having well and uniquely defined 3D points to perform comparisons between flat and dome port underwater surveys. The relative positions of the targets on the plates are known by laboratory calibration, thus by measuring at least three non-collinear targets in the underwater or above the water photogrammetric surveys, the 3D coordinates of the remaining targets can be computed through a similarity transformation. By means of this procedure, common points between underwater and above the water surveys can be derived and the two 3D models are registered together. Some tape length measurements are used to scale the object.

(**a**) (**b**)

Figure 9. Plates with coded targets used in the experiment (**a**). An aerial view of the port structure with an enlarged sight of the rectangular basin chosen for the tests with a schematic view of the photogrammetric strip acquired (**b**).

5.3. Planning and Acquisition of the Underwater and Above-The-Water Camera Network

Since the results of the preliminary calibrations showed a significant different behaviour of the two ports, a much evident discrepancy between the two would be expected in elongated strips, such as those needed for surveying big structures. Indeed, systematic residual errors that are not properly modelled by camera calibration parameters are expected to accumulate along the strip, thus leading to global object deformation (Nocerino et al., 2014).

The camera network planned to survey the rectangular basin consists in a singular open loop strip taken at about 2 m from the vertical walls with the dome port, and 2.6 meters with the flat port to obtain a GSD of about 0.5 mm in both cases. 80% overlap was considered along the strip and some convergent and rolled images were acquired to improve the self-calibration (especially considering the geometric characteristics of the object that results flat within the field of view of the single images). The image acquisitions (Figure 10a) were carried out in sequence, the dome port first and the flat port soon after. The maximum depth was 1.5m, water temperature about 15 degrees, and the underwater image acquisition required about three hours in total. The part above the water was surveyed with the same camera without the pressure housing. The available side walking path was used to photograph the structure on the opposite side, thus leading to an average distance to the object of about 12 m (GSD about 3 mm). Same 80% overlap with rolled and convergent image acquisition protocol was used above the water.

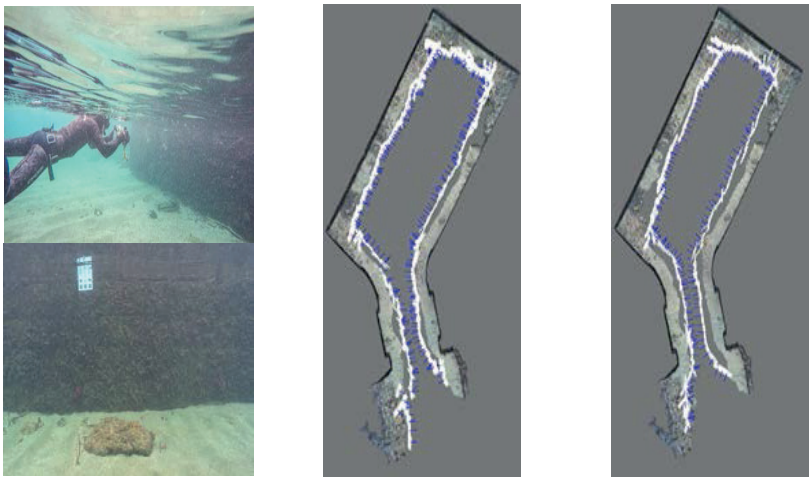

(**a**) (**b**) (**c**)

Figure 10. Underwater image acquisition and a sample image from the dome port (**a**). Final camera networks for the dome port (**c**) and flat port (**d**).

5.4. Self-Calibrating Bundle Adjustment

The three image datasets, two underwater and one above the water, were processed with the same procedure. The images were automatically oriented using Agisoft PhotoScan where self-calibration with radial and decentering distortion parameters were computed. The final camera network for the dome and flat ports is shown in Figure 10 (b-c).

A preliminary comparative analysis of the bundle adjustment parameters that were retrieved by PhotoScan for the two underwater datasets confirmed a less precise solution with the flat port.

A very important difference was observed on the self-calibration parameters. While for the dome port the standard deviations for the focal length is 0.4 μm, for the flat port the standard deviation resulted more than three times worse, i.e., 1.4 μm. In general, the self-calibration parameters of the flat port were an order of magnitude worse than those that were computed for the dome port. Such a worse precision is expected to be a source of systematic errors that accumulates along the photogrammetric strip and "vent" into the object space leading to a stronger global deformation of the 3D model for the flat port. Therefore, as shown in Nocerino et al. (2014), over the 70 meters linear perimeter of the underwater basin, the global deformations can reach some centimetres, even if the GSD is sub-millimetric.

For the above the water dataset, as expected, the precision of calibration parameters was much greater, providing a standard deviation for the focal length of some 0.1 μm, which is more than ten times better than that of the flat port underwater. The three datasets were scaled using a combination of length measurements that were provided by the plates and some tape measurements. A maximum scaling error of about 0.2% was estimated from the residuals on the reference known lengths.

The approach described in Nocerino et al. (2014) was employed to further analyse the three processings, namely the above the water (no port) and underwater, with both dome and flat ports, acquisitions. The tie points extracted in PhotoScan were imported in PhotoModeler Scanner where a bundle adjustment was executed and the precision vector length of the 3D object coordinates of the triangulated tie points are shown in Figure 11 for the three different acquisitions.

The precision vector length is the square root of the sum of the squared theoretical precision of the coordinates in the three directions. It is the expected variability of estimated 3D object coordinates, resulting from the adjustment process and depending on camera network and precision of image observations.

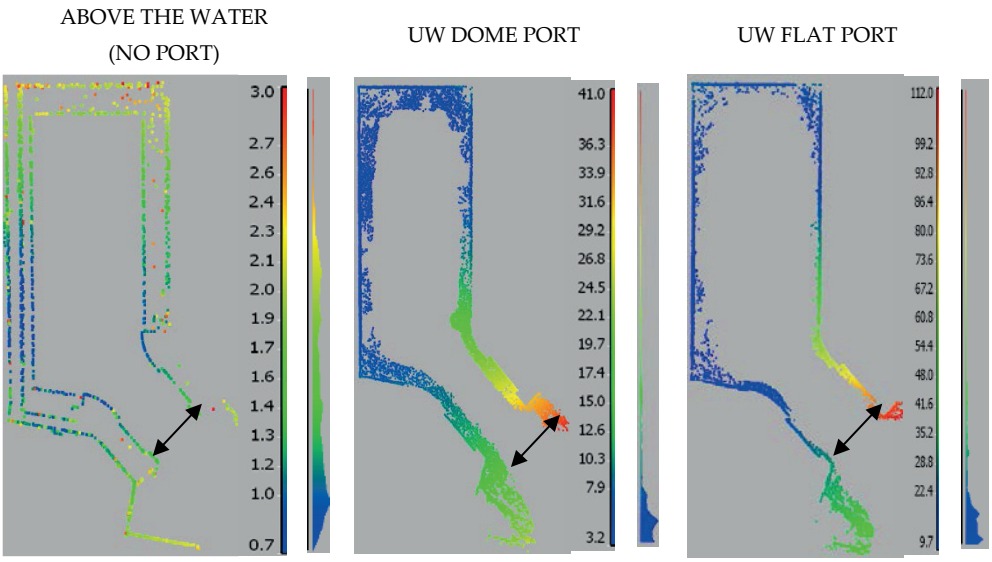

Figure 11. Three-dimensional (3D) tie point cloud coloured according to the precision vector length in mm for above the water (no port) and underwater acquisitions, with both dome and flat ports. Black arrows show where reference measurement was taken.

The precision is computed according to error propagation theory. The theoretical precision would coincide with the accuracy of object coordinates if all of the systematic errors had been properly modelled.

Three are the most remarkable outcomes. It is worth noting that the expected precision for the above the water survey is two to three orders of magnitude better than the underwater cases. The behaviour of the precision distribution is very similar for the two underwater acquisitions, where a significant degradation at the extremities of the structure is visible (the different histogram ranges of colour scales in figure 11 were chosen to highlight the weak point of each photogrammetric processing). However, the theoretical precision of the dome port is determined to three times better than that of the flat port.

Table 4. Statistics of 3D precision vector length for the different solutions.

Precision Vector Length	**D750-24mm *No Port* above Water**	**D750-24mm *Dome Port* UW**	**D750-24mm *Flat Port* UW**
MIN [mm]	0.7	3.2	9.7
MAX [mm]	3.0	41.0	112.0
MEAN [mm]	1.5	10.5	27.2
RMS [mm]	0.5	8.3	22.6

5.5. Accuracy and 3D Analysis in Object Space

A simple evaluation was carried out to assess the accuracy of the two underwater surveys. A reference distance by tape measurement (estimated accuracy ca. 1cm) was taken between the two plates facing each other at the entrance of the rectangular basin (black arrows in Figure 11) and compared with those obtained from the underwater survey (Table 5). Being the two plates at the beginning and end of the strip, the resulting discrepancy can be considered as a loop closure error. An error about 30 cm was observed for the flat port.

Table 5. Summary of length check.

Reference Distance	**D750-24mm *Dome Port* UW**	**D750-24mm *Flat Port* UW**
4.723 m	4.729 m	5.015 m
Error→	**0.006 m (≈12xGSD)**	**0.292 m (≈600xGSD)**

5.6. Photogrammetric Processing of the Single R, G, B Channels

As already mentioned in Section 4.3.1, the three channels for the flat port display different image quality, especially at the corners.

The three R, G, B channels for both the flat port and dome port were extracted from the RGB images and were saved as single channel images to be processed separately.

For the flat port, only the Red and Green channels succeeded the orientation stage. On the contrary, the images in the Blue channel probably appeared too blurred and were only partially oriented. The three channels for the dome port were oriented without any difficulty.

As the images in the three channels were acquired from the same position and exactly with the same camera network, the results in object space are expected not to be significantly different. An inner comparison between the three channels of each port was performed by comparing the 3D coordinates of the plates that were obtained separately from each channel. According to PhotoScan manual, the default processing considers a combination of the three R, G, B channels. Consequently, the previous results (Sections 5.4 and 5.5), obtained in default mode, were used as reference for the relative comparisons between the different colour channels.

A similarity transformation with isotropic scale factor was computed to compare the 3D coordinates. The Euclidean distances between same points are used as a measure of discrepancy. Table 6 summarizes the relative comparison for each channel and port reported as RMS and maximum discrepancy between 3D points. A maximum difference of 23 cm was observed between the red channel of the flat port and the RGB combination for the same flat port. The solutions between the three channels of the dome port proved more consistent among themselves,

meaning that the 3D shape is much more invariant for the dome port when different single channels are used.

Table 6. Summary of the relative comparison between 3D coordinates obtained from the single R,G,B channels and the one obtained as RGB combination for each port.

	D750-24mm *dome port* UW		**D750-24mm *flat port* UW**	
	RMS [m]	**Max [m]**	**RMS [m]**	**Max [m]**
RED	0.005	0.013	0.096	0.229
GREEN	0.003	0.006	0.023	0.055
BLUE	0.010	0.023	n/a	n/a

The accuracy analysis shown in Section 5.5 was repeated for the different colour channels for both ports. Since the blue channel images were not successfully oriented, only the error for the red and green channels were reported in Table 7 for the flat port. The discrepancy between the reference distance and the one measured in the green channel of the flat port reduced from 29 to 22 cm, and from 29 to 7 cm for the red channel. Slight variations were seen for the dome port, with the blue channel behaving the worst again.

Table 7. Summary of the loop closure error for both dome and flat ports (reference distance: 4.723 m).

D750-24mm *dome port* UW				
	RGB	**RED**	**GREEN**	**BLUE**
Measured distance	4.729 m	4.725 m	4.718 m	4.766 m
Error	0.006 mm (≈12xGSD)	0.002 m (≈4xGSD)	−0.005 m (≈10xGSD)	−0.043 m (≈86xGSD)
D750-24mm *flat port* UW				
	RGB	**RED**	**GREEN**	**BLUE**
Measured distance	5.015 m	4.656	4.940	n/a
Error	0.292 m (≈580xGSD)	−0.067 m (≈134xGSD)	0.217 m (≈434xGSD)	n/a

5.7. 3D Modelling of the Structure

Dense point clouds were computed at 1/8 and ¼ linear resolution, respectively, for the dome port and the above-the-water photogrammetric surveys corresponding to a spatial resolution of 4 mm in the object space. An optimized mesh according to Rodriguez et al. (2015) was wrapped over the manually cleaned point clouds for each dataset. The joint alignment procedure presented in Menna et al. (2015, 2013) was used to register the underwater mesh with the one above the water. The RMS of the transformation was some 3 cm for the dome port and 13 cm

for the flat port. Figure 12 shows some renderings of the basin after the alignment of the underwater (dome port) and above-the-water 3D models.

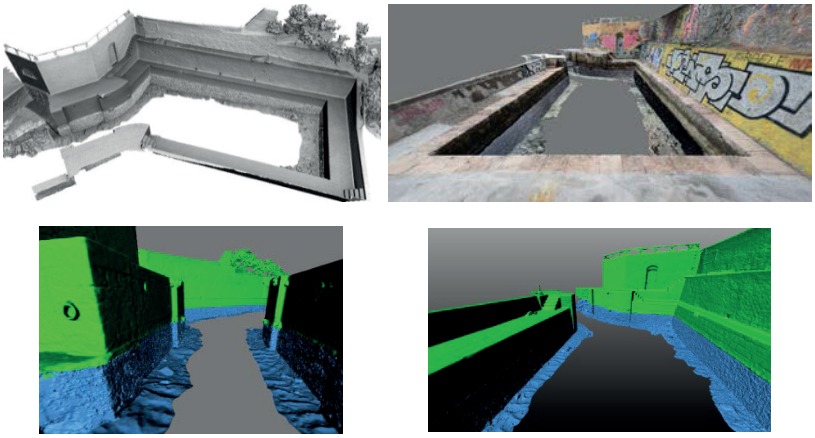

Figure 12. Renderings of the basin after the alignment of the underwater and above-the-water 3D models.

6. Concluding Remarks

This paper investigated the effect of the diverse image quality of flat and dome ports over the accuracy of the final 3D model obtained through photogrammetric procedures. The paper highlighted the influence of image quality over the global accuracy of the final 3D model. Image quality underwater undergoes a very evident degradation due to the sum of optical phenomena, arising from both the pressure housing and port used and the physical and environmental properties of water itself. Indeed, due to the combination of optical aberrations, such as astigmatism, heavy distortions, and chromatic aberrations, plus a non-complete modelling of unknown systematic image errors, strong global deformations were observed and assessed through both off the internal parameters that were provided by the bundle adjustment and simple length measurements for the two ports. A very high error of some 29 cm was found with the flat port data set. Preliminary calibrations on a portable test object anticipated a degradation of accuracy when using the flat port by reporting high RMS of image residuals, a less precise calibration (worse standard deviations for camera parameters), and a lower 3D point precision in object space. A significant different image quality per colour channel was observed. From the visual inspection of the images, the red channel resulted less influenced by blur effects towards the corners showing a higher contrast and sharpness across the whole sensor format. Different photogrammetric processing for each colour were carried out to investigate how the different image quality affects the final metric results. RGB combination was compared against the single red, green, and blue channels. As expected, the green channel performed

more similarly to the RGB combination than the other channels, as the digital sensor of the Nikon D750 uses the Bayer filter array. The red channel provided a significant improved accuracy with respect to the processing that was obtained from the combination of the R, G, B channels. The blue channel proved to be the most problematic and might probably degrade the accuracy when combined with the other channels. This test was important because software applications may combine the three channels by default, which may not be the best procedure for underwater photogrammetry.

The issues raised by this study may deserve more experimental tests for example using different housings and ports. Having observed a strong difference between image quality between the centre and corners, successive tests will take into account a different weighting for image observations according to optical quality parameters (e.g. Modulation Transfer Function-MTF).

References

1. Austin, R.W.; Halikas, G. *The Index of Refraction of Seawater*; SIO Ref. No. 76–1; National Technical Information Service: Springfield, VA, USA, January 1976.
2. Balletti, C.; Beltrame, C.; Costa, E.; Guerra, F.; Vernier, P. Underwater photogrammetry and 3D reconstruction of marble cargos shipwreck. *Int. Arch. Photogramm. Remote Sens. Spat. Inf. Sci.* **2015**, *40*, 7.
3. Börlin, N.; Grussenmeyer, P. Bundle adjustment with and without damping. *Photogramm. Rec.* **2013**, *28*, 396–415.
4. Cialdi, A.; Secchi, P.A. Sur la transparence de la mer. *Comptes Rendus Hebdomadaire de Séances de l'Academie des Sciences* **1865**, *61*, 100–104.
5. Ciompi, L. Dalla costa fiorita di Quercianella. Edizione Stella del Mare Livorno. 1991. Available online: http://www.quercianellasonnino.it/bibliografia.php (accessed on 3 May 2017).
6. Demesticha, S.; Skarlatos, D.; Neophytou, A. The 4th-century BC shipwreck at Mazotos, Cyprus: new techniques and methodologies in the 3D mapping of shipwreck excavations. *J. Field Archaeol.* **2014**, *39*, 134–150.
7. Diamanti, E.; Vlachaki, F. 3D Recording of Underwater Antiquities in the South Euboean Gulf. The International Archives of Photogrammetry. *Remote Sens. Spat. Inf. Sci.* **2015**, *40*, 93.
8. Floor, J.A. Water and Light in Underwater Photography. 2005. Available online: http://www.seafriends.org.nz/phgraph/water.htm.
9. Fraser, C.S. Digital camera self-calibration. *ISPRS J. Photogramm. Remote Sens.* **1997**, *52*, 149–159.
10. Kwasnitschka, T.; Köser, K.; Sticklus, J.; Rothenbeck, M.; Weiß, T.; Wenzlaff, E.; Schoening, T.; Triebe, L.; Steinführer, A.; Devey, C.; et al. DeepSurveyCam—A deep ocean optical mapping system. *Sensors* **2016**, *16*, 164.

11. Helmholz, P.; Long, J.; Munsie, T.; Belton, D. Accuracy assessment of GOPRO Hero 3 (Black) camera in underwater environment. *Int. Arch. Photogramm. Remote Sens. Spat. Inf. Sci.* **2016**, *41*, 477–483.
12. Luhmann, T.; Hastedt, H.; Tecklenburg, W. Modelling of chromatic aberration for high precision photogrammetry. *Int. Arch. Photogramm. Remote Sens. Spat. Inf. Sci.* **2006**, *36*, 173–178.
13. Luhmann, T.; Robson, S.; Kyle, S.; Boehm, J. *Close-Range Photogrammetry and 3D Imaging*; Walter de Gruyter: Berlin, Germany, 2014.
14. Matsuoka, R.; Asonuma, K.; Takahashi, G.; Danjo, T.; Hirana, K. Evaluation of correction methods of chromatic aberration in digital camera images. *ISPRS Ann. Photogramm. Remote Sens. Spat. Inf. Sci.* **2012**, *I-3*, 49–55.
15. McCarthy, J.; Benjamin, J. Multi-image photogrammetry for underwater archaeological site recording: an accessible, diver-based approach. *J. Marit. Archaeol.* **2014**, *9*, 95–114.
16. Menna, F.; Nocerino, E.; Fassi, F.; Remondino, F. Geometric and optic characterization of a hemispherical dome port for underwater photogrammetry. *Sensors* **2016**, *16*, doi:10.3390/s16010048.
17. Menna, F.; Nocerino, E.; Troisi, S.; Remondino, F. Joint alignment of underwater and above-the-water photogrammetric 3D models by independent models adjustment. *Int. Arch. Photogramm. Remote Sens. Spat. Inf. Sci.* **2015**, *40*, 143.
18. Menna, F.; Nocerino, E.; Troisi, S.; Remondino, F. A photogrammetric approach to survey floating and semi-submerged objects. *Proc. SPIE* **2013**; *8791*, doi:10.1117/12.2020464.
19. Nocerino, E.; Menna, F.; Fassi, F.; Remondino, F. Underwater calibration of dome port pressure housings. *Int. Arch. Photogramm. Remote Sens. Spat. Inf. Sci.* **2016**, *40*, 127–134.
20. Nocerino, E.; Menna, F.; Remondino, F. Accuracy of typical photogrammetric networks in cultural heritage 3D modeling projects. *Int. Arch. Photogramm. Remote Sens. Spat. Inf. Sci.* **2014**, *40*, 465–472.
21. Roman, C.; Mather, R. Autonomous underwater vehicles as tools for deep-submergence archaeology. Proceedings of the institution of mechanical engineers. *Part M J. Eng. Marit. Environ.* **2010**, *224*, 327–340.
22. Reznicek, J.; Luhmann, T.; Jepping, C. Influence of raw image preprocessing and other selected processes on accuracy of close-range photogrammetric systems according to VDI 2634. *Int. Arch. Photogramm. Remote Sens. Spat. Inf. Sci.* **2016**, *41*, 107–113.
23. Robson, S.; MacDonald, L.; Kyle, S.A.; Shortis, M.R. Multispectral calibration to enhance the metrology performance of C-mount camera systems. *Int. Arch. Photogramm. Remote Sens. Spat. Inf. Sci.* **2014**, *40*, 517.
24. Rodríguez-Gonzálvez, P.; Nocerino, E.; Menna, F.; Minto, S.; Remondino, F. 3D surveying & modeling of underground passages in WWI fortifications. *Int. Arch. Photogramm. Remote Sens. Spat. Inf. Sci.* **2015**, *40*, 17–24.
25. Shortis, M. Calibration techniques for accurate measurements by underwater camera systems. *Sensors* **2015**, *15*, 30810–30826.
26. Telem, G.; Filin, S. Photogrammetric modeling of underwater environments. *ISPRS J. Photogramm. Remote Sens.* **2010**, *65*, 433–444.

Menna, F.; Nocerino, E.; Remondino, F. Photogrammetric Modelling of Submerged Structures: Influence of Underwater Environment and Lens Ports on Three-Dimensional (3D) Measurements. In *Latest Developments in Reality-Based 3D Surveying and Modelling*; Remondino, F., Georgopoulos, A., González-Aguilera, D., Agrafiotis, P., Eds.; MDPI: Basel, Switzerland, 2018; pp. 279–303.